

Synthesis of mesoporous SnO₂ nanomaterials with selective gas-sensing properties

Lei Li · Huiming Lin · Fengyu Qu

Received: 20 April 2013 / Accepted: 7 July 2013 / Published online: 23 July 2013
© Springer Science+Business Media New York 2013

Abstract Using SBA-15/KIT-5/KIT-6 as the hard templates, the mesoporous SnO₂ nanomaterials with different structures were synthesized by nanocasting. X-ray diffraction, transmission electron microscopy, and nitrogen adsorption isotherms were used to testify their structure characteristics. These mesoporous SnO₂ nanomaterials showed high specific surface areas (57–96 m² g⁻¹) and pore volume (0.17–0.27 cm³ g⁻¹). The nanopore of these templates makes the nanosize particle of the final mesoporous SnO₂ nanomaterials (4–9 nm) at last. The sensing properties of acetone, ethyl alcohol and methyl alcohol were investigated. The response of SnO₂-15, SnO₂-5, and SnO₂-6 are 17.0, 19.5, and 16.1, respectively as the concentration of ethyl alcohol on 200 ppm. The sensitivity of SnO₂-5 is 28.2 as the concentration of acetone was increased to 200 ppm. With the large surface area, high pore volume, and nanosized particles (close to 2 L = 6 nm of SnO₂), the SnO₂-5 show four fold enhancement in sensitivity compared to commercial SnO₂ powder and low detection limit (even at 200 ppb). The surface area and particle size play a significant party in the gas response. With the large surface area and smallest particle size, SnO₂-5 shows the highest sensitivity of all. These mesoporous nanomaterials show well potential application on the gas response.

Keywords SnO₂ · Mesoporous · Replicated synthesis · Gas sensor

1 Introduction

Since the successful synthesis of MCMs in 1992 [1, 2], mesoporous materials have attracted much attentions due to their highly ordered structure, tunable pore size, high pore volume, and large surface area [3–7]. These materials have been widely used in adsorption, separation, nano-reactors, drug carriers, and catalysis etc. Owing to the special structure advantages, mesoporous silica materials were usually used as the host to disperse the guest components to improve their properties on various practical applications. Li and Kawi [8] utilized MCM-41 as a support to mechanically mix with SnO₂, and the sensitivity of the resulting sensor to H₂ could be enhanced compared with that of pure SnO₂ gas sensor.

Considering the advantage of mesoporous structure materials, the mesoporous materials of carbon, organic compound, metal oxide, and metal sulfide also have been synthesized, followed the mesoporous silica materials. Ryoo's group reported the preparation of the ordered mesoporous carbon using highly ordered mesoporous silica [9]. With the excellent optical and electric properties, the synthesis of mesoporous semiconductor metal oxide has become research focus on catalysis, electrics, and gas sensor etc.

Generally, there are two ways to synthesize the mesoporous metal oxide, including soft template and hard template methods. For the soft template method, the surfactant was used as the template by solvent evaporation method. After calcinations to remove the surfactant, the mesoporous structures are disordered and collapsed easily

L. Li · H. Lin · F. Qu (✉)
Key Laboratory of Photonic and Electronic Band Gap Materials,
Ministry of Education, College of Chemistry and Chemical
Engineering, Harbin Normal University, Harbin 150025,
People's Republic of China
e-mail: qufengyuchem@yahoo.com.cn

L. Li
e-mail: leilei82701334@163.com

[10]. For the hard template method, mesoporous carbon materials were usually for mesoporous metal oxide because the carbon can be removed under calcinations and the metal oxide framework remained. But the hydrophobic property of carbon always makes it difficult for mesoporous carbon material to be filled with the metal precursor completely. Huang et al. [11] used SBA-15 as template to successfully synthesize In_2O_3 nanorods mesoporous materials with diameter of about 7 nm. Wagner et al. [12] synthesized mesoporous ZnO successfully.

SnO_2 , an n-type semiconductor with a wide band-gap ($E_g = 3.6$ eV), has been widely used in solar cells [13–16], catalysis [17–19], and gas sensors [20–29]. To increase the efficiencies for these applications [30–32], mesoporous structure SnO_2 is required to provide an enhanced the surface area and pore volume. Most previous efforts [18, 19, 25–29, 33] are focused on the study of structure and component-dependent properties. Therefore, it is meaningful to study the gas-sensing properties of mesoporous SnO_2 .

In this paper, SBA-15, KIT-5, and KIT-6 were employed as the hard templates to replicate the mesoporous SnO_2 nanomaterials with different structure. These mesoporous nanomaterials were characterized by power X-ray diffraction (XRD), N_2 adsorption and desorption, and transmission electron microscope (TEM), and Raman. The sensing properties of these mesoporous SnO_2 nanomaterials to ethanol, methanol and acetone were detected in detail. And sensor mechanisms were discussed as well.

2 Experimental

2.1 Chemicals

Poly(ethylene glycol)-block-poly(propylene glycol)-block-poly(ethylene glycol) triblock copolymer Pluronic P123 ($M_w = 5,800$, $\text{EO}_{20}\text{PO}_{70}\text{EO}_{20}$) was purchased from Aldrich Corp. Pluronic F127 triblock copolymer $[(\text{HO}(\text{CH}_2\text{CH}_2\text{O})_{106}-(\text{CH}_2\text{CH}(\text{CH}_3)\text{O})_{70}-(\text{CH}_2\text{CH}_2\text{O})_{106}\text{H}, \text{EO}_{106}\text{PO}_{70}\text{EO}_{106}]$ was purchased from Sigma. $\text{SnCl}_4 \cdot 5\text{H}_2\text{O}$ was purchased from Guoyao Chemical Co. HCl was purchased from Guangfu Industry of Fine Chemicals Institute, Tianjin. H_2SO_4 , was purchased from Fuchen Chemical Co., Tianjin. Tetraethyl orthosilicate (TEOS) was purchased from Tiantai Chemical Co., Tianjin. $\text{C}_4\text{H}_{10}\text{O}$ was purchased from Guangfu Industry of Fine Chemicals Institute, Tianjin. NaOH was purchased from Dalu Chemical Co., Tianjin. Commercial SnO_2 powder was purchased from Guangfu Industry of Fine Chemicals Institute, Tianjin.

All chemicals were analytical reagents and used as received without any further treatment. Deionized water was used in all experiments.

2.2 Preparation of template

SBA-15 was synthesized by using a non-ionic oligomeric alkyl-ethylene oxide surfactant (Pluronic 123) as the structure directing agent [34]. 4 g of P123 was dissolved in 30 g of deionized water with stirring. After the polymer had been dissolved, 120 g of 2 M HCl solution, and 8.5 g of tetraethyl orthosilicate (TEOS) was added under stirring at room temperature. After the system was further stirred at 35 °C for 20 h, the mixture was transferred into an oven at 100 °C for 2 days. And then, filtrated and washed by plenty of deionized water and dried. Calcinations at 550 °C for 5 h in air remove the surfactant (SBA-15).

KIT-6 [35] was synthesized by using P123 as the structure directing agent. 6 g of P123 was dissolved in 217 g of deionized water and 10 ml HCl solution, and then 6 g of butanol ($\text{C}_4\text{H}_{10}\text{O}$) was added under stirring at 35 °C. After stirring 1 h, 12.9 g of tetraethyl orthosilicate (TEOS) was added. The mixture was left under stirring for 24 h. Then the mixture was transferred into an oven at 100 °C for 1 day. Upon cooling down to room temperature, filtrated, and washed by HCl and $\text{C}_2\text{H}_5\text{OH}$, dried. Then calcinations at 550 °C for 5 h in air remove the template.

KIT-5 [36] was synthesized by using F127 as the structure directing agent. 5 g of F127 was dissolved in 240 g of deionized water and 10.5 ml HCl solution. Then 24 g of TEOS was added under stirring at 45 °C. After stirring 24 h, the mixture was transferred into an oven at 100 °C for 1 day. Upon cooling down to room temperature, filtrated, and washed by plenty of deionized water, dried. Then calcinations at 550 °C for 5 h in air remove the template.

2.3 Synthesis of mesoporous SnO_2 nanomaterials

$\text{SnCl}_2 \cdot 2\text{H}_2\text{O}$ was dissolved in 10 g of ethanol. This solution was mixed with 1 g of the template and stirred at room temperature until all of the solution was adsorbed. After drying at room temperature, this process (impregnation and drying) was repeated to obtain the SnO_2 precursor/ SiO_2 . The composite was further annealed at 500 °C for 3 h and the silica template was removed from the $\text{SnO}_2/\text{SiO}_2$ composite by treating with dilute 2 M NaOH solution for 6 h and washing with deionized water and ethanol several times. The mesoporous SnO_2 nanomaterials replicated from SBA-15, KIT-5, and KIT-6 are named as SnO_2 -15, SnO_2 -5, and SnO_2 -6, respectively.

2.4 Measurement of gas sensing properties

The as-synthesized sample was mixed with deionized water to form the paste. The paste was coated on a ceramic tube on which a pair of gold electrodes, and then a Ni-Cr

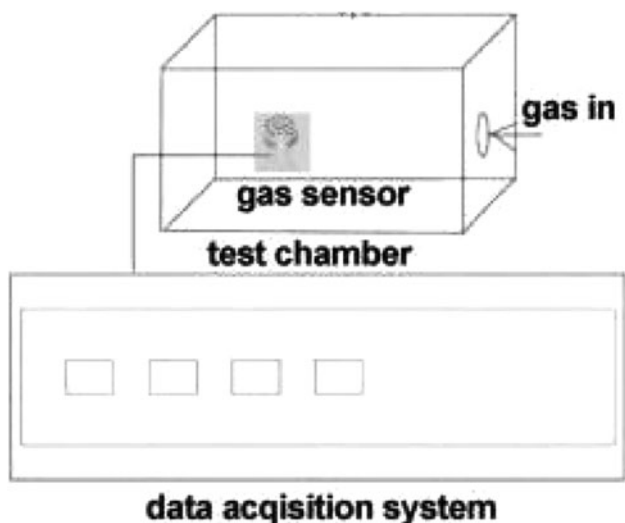


Fig. 1 A schematic diagram of the experimental setup

heating wire was inserted in the tube to form a side-heated gas sensor.

Gas sensing properties were measured using a static test system which included a test chamber and a data acquisition/processing system. Dry air was used as both a reference gas and a diluting gas to obtain desired concentrations of target gases. The target gas was injected into the test chamber by a syringe through a rubber plug. When the response reached a constant value, the sensor was taken out to recover in dry air and the experiments were repeated. The gas response was defined as R_a/R_g , where R_a and R_g are the resistances of the sensor upon exposure to dry air and target gas, respectively. The response time was specified as the time to rise to 90 % of the equilibrium value of sensor resistance after target gas was injected. The recovery time was defined as the time to fall to 10 % of the final resistance value after the removal of target gas [37]. In this paper, we selected 1 L volume jars for response and

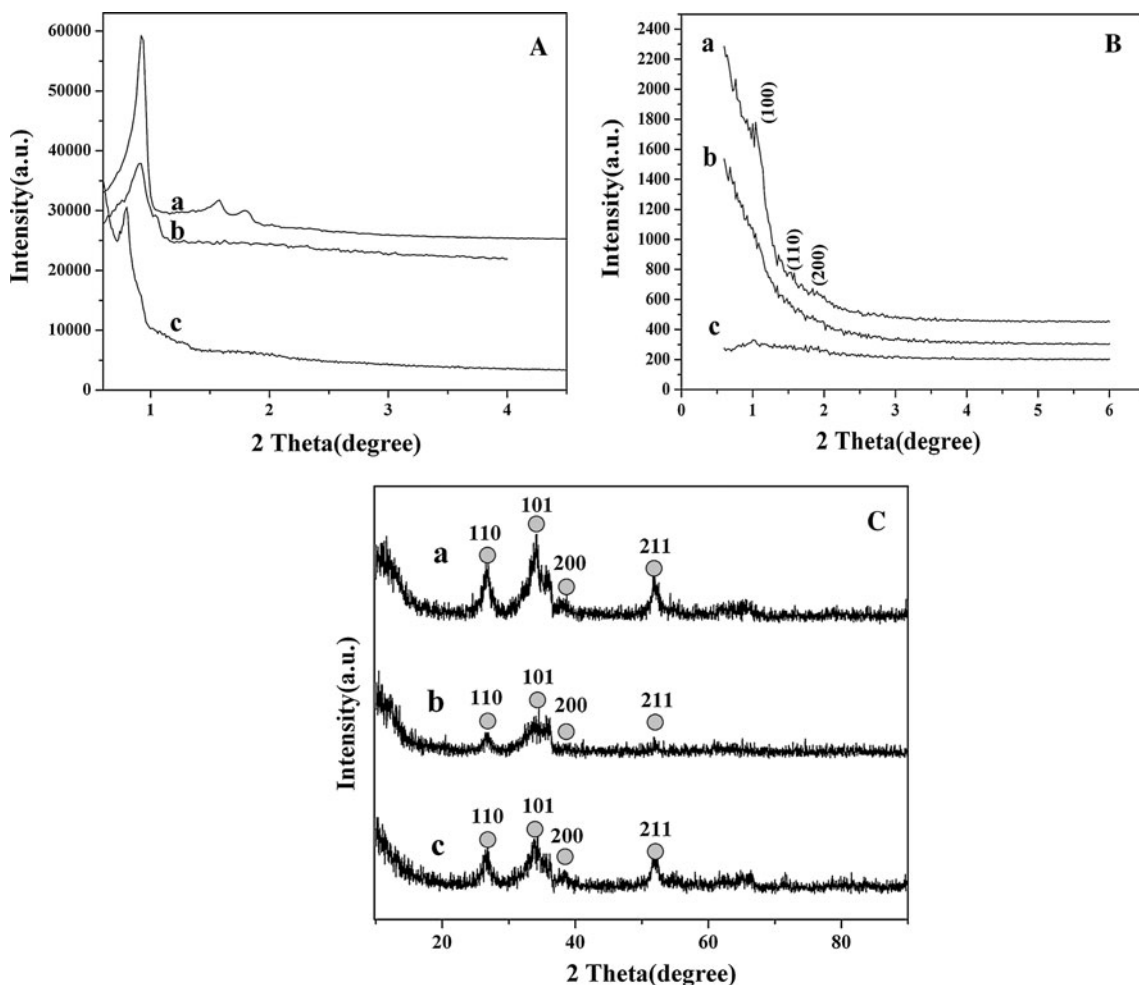


Fig. 2 a Small-angle XRD patterns of a SBA-15, b KIT-5 and c KIT-6; b Small-angle XRD patterns of a SnO₂-15, b SnO₂-5 and c SnO₂-6 and C Wide-angle XRD patterns of a SnO₂-15, b SnO₂-5 and c SnO₂-6

recovery time measurement. And we put the sensor into the jars after the gas concentration reach equilibrium and remove it into air jar after test. A schematic diagram of the experimental setup are shown in Fig. 1.

2.5 Characterization

X-Ray Diffraction data were collected on a SIEMENS D 5005 diffractometer with Cu K α , using a radiation at 40 kV and 30 mA. The nitrogen adsorption/desorption, surface areas, and median pore diameters were measured using a Micromeritics ASAP 2010 M sorptometer. Before measured at 77 K, the samples were degassed at 473 K for 12 h. Specific surface areas and pore size distributions were calculated using the Brunauer–Emmett–Teller (BET) and Barrett–Joyner–Halenda (BJH) models from the adsorption branches, respectively. TEM images were recorded on JEOL 3010. The Raman spectrum was measured on a VERTEX-70 BRUKER RAM II spectrophotometer with an Nd:YAG laser at the excitation wavelength of 1,064 nm.

3 Results and discussion

3.1 Structural

Figure 2A shows small-angle XRD patterns of SBA-15, KIT-5, and KIT-6. As shown in Fig. 2a, it exhibits three

Table 1 Textural properties of the ordered mesoporous SnO₂ nanomaterials

Sample	S _{BET} m ² g ⁻¹	Pore volume cm ³ g ⁻¹	Pore diameter nm
SnO ₂ -15	96	0.21	3.7
SnO ₂ -5	77	0.27	3.8
SnO ₂ -6	57	0.17	3.5

well-resolved peaks corresponding to the (100), (110), and (200) typical diffractions of 2D-hexagonal symmetry [38]. Figures 2b and 2c display the cubic *Im* $\bar{3}m$ and *Ia* $\bar{3}d$ structured KIT-5 and KIT-6, both possess highly ordered mesoporous structures. Figure 2B shows small-angle XRD pattern of SnO₂ samples. The (100), (110), and (200) diffractions are observed, implying SnO₂-15 replicated the structure of SBA-15. While for SnO₂-5 and SnO₂-6, the peak intensity is weaker, exhibiting the less ordered mesoporous structure. Figure 2C reveals the wide-angle XRD patterns of SnO₂-15, SnO₂-5, and SnO₂-6 composites. The peaks at 26.8°, 34.1°, 38.6°, and 51.9° is ascribed to the typical (110), (101), (200), and (211) diffractions of rutile structure of SnO₂ (JCPDS 41-1445). No diffraction peaks from any other impurities are detected.

The nitrogen adsorption isotherms of mesoporous SnO₂ nanomaterials are shown in Fig. 3a. All sample show the typical IV isotherm curve, revealing the mesoporous structure of them. This is consistent with the small angle XRD pattern as described above. Figure 3b shows the BJH pore diameter distribution of these samples, demonstrating the uniform pore distribution of them. As calculated by the BJH method from the desorption branch of the nitrogen isotherm, the corresponding pore diameter is 3.7, 3.8, 3.5 nm for SnO₂-15, SnO₂-5 and SnO₂-6, respectively. The structure features of all the nanomaterials are summarized in Table 1. The BET surface areas and pore volumes of them are 96 m²g⁻¹ and 0.21 cm³g⁻¹, 77 m²g⁻¹ and 0.27 cm³g⁻¹, and 57 m²g⁻¹ and 0.17 cm³g⁻¹, respectively. With the mesoporous structure, all the samples have the large surface area and high pore volume compared with other common SnO₂ materials [39].

The detailed microstructures of the as-synthesized mesoporous SnO₂ nanomaterials were investigated by TEM. The TEM images of SnO₂-15, SnO₂-5 and SnO₂-6 are shown in Fig. 4a–i. From the Fig. 4a, b, the typical stripe-

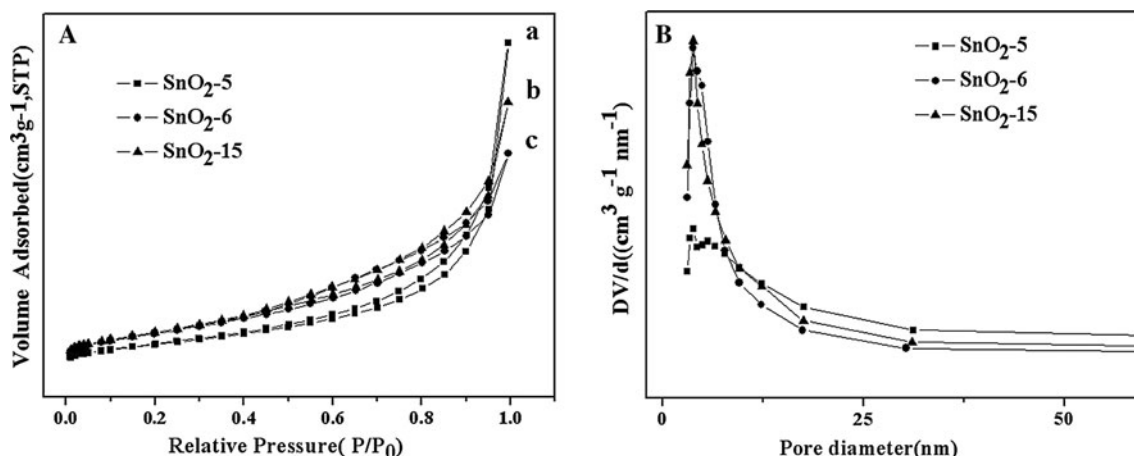


Fig. 3 Nitrogen adsorption–desorption isotherms **a** and pore diameter distribution curves **b** of mesoporous SnO₂ nanomaterials

like and hexagonally arranged TEM images, viewed from the [100] and [110] directions, are observed in SnO₂-15. And their particle size is about 7–9 nm. From Fig. 4d, e, g, h, SnO₂-5 and SnO₂-6 show the less ordered structure with the particles size of 4–6 nm and 5–7 nm, respectively. After the removing of the template, the mesoporous structure damage in SnO₂-5 and SnO₂-6. A high resolution TEM images (Fig. 4c, f, i) show the clearly lattice fringes with d spacing values are calculated to be about 0.34 and 0.26 nm, corresponding to (110) and (101) planes of SnO₂ nanomaterials.

Raman scattering is a useful tool for the characterization of nanosized nanomaterials and a qualitative probe of the presence of lattice defects in solids [40]. Meanwhile, the Raman spectrums of mesoporous SnO₂ nanomaterials are shown in Fig. 5. As in Fig. 5, three Raman active peaks located at 631, 777 and 475 cm⁻¹ are consistent with the

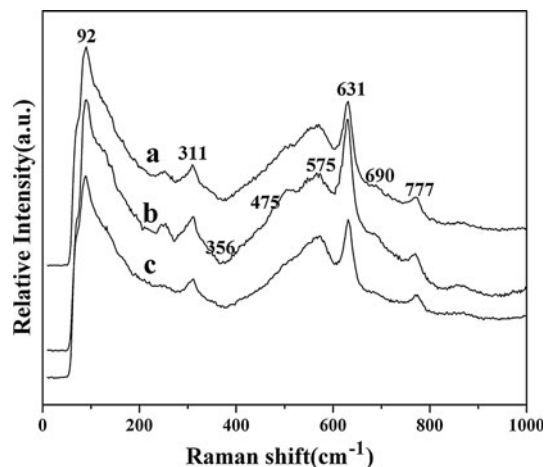


Fig. 5 Raman spectrum of a SnO₂-15, b SnO₂-5, and c SnO₂-6

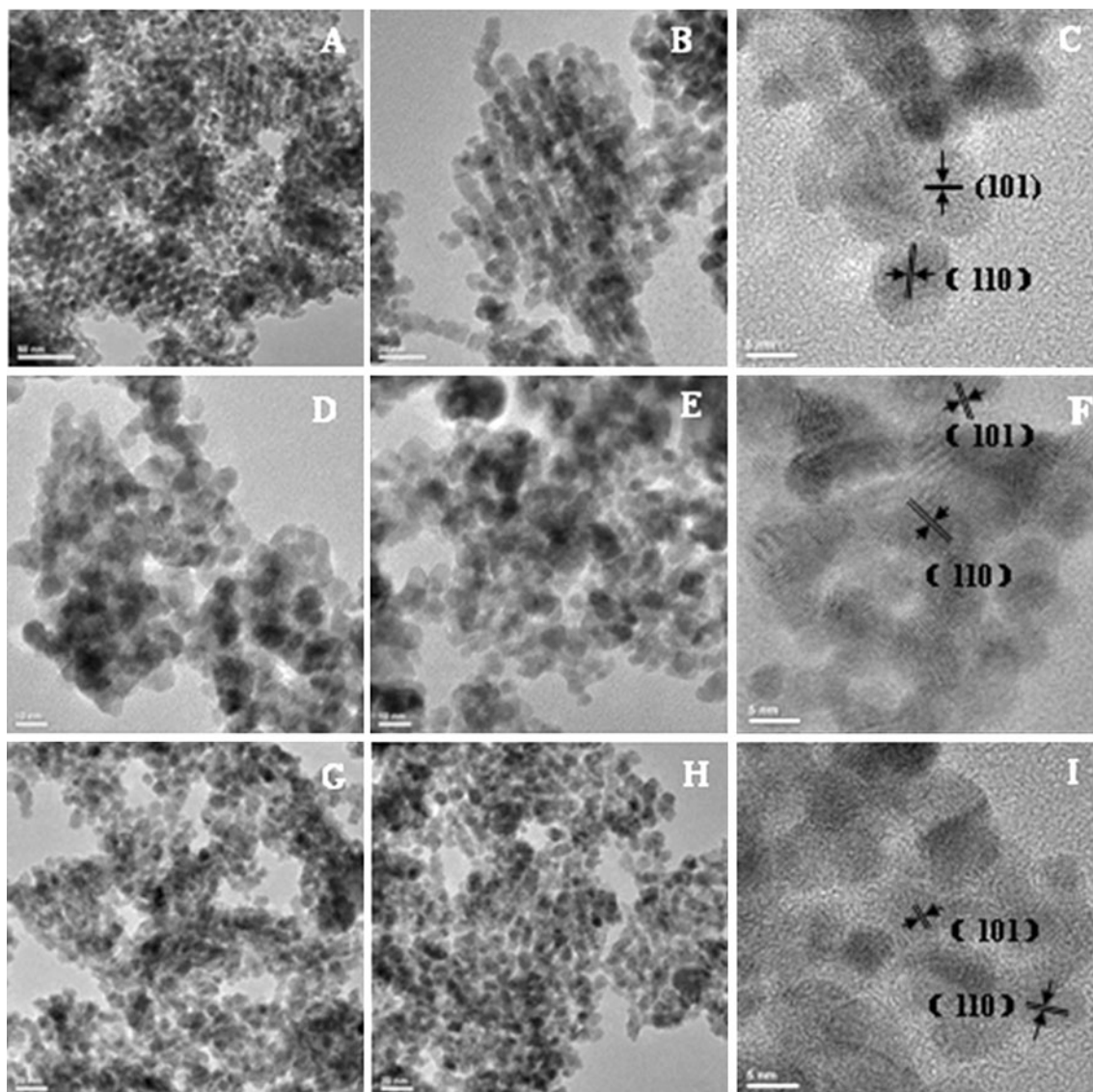


Fig. 4 TEM images of a–c SnO₂-15, d–f SnO₂-5 and g–i SnO₂-6

A_{1g} , B_{2g} and E_g vibration modes respectively. Besides, we also observed other Raman peaks of 354 (N_1) and 575 (N_2) cm^{-1} , which can be assigned to the surface defects of the SnO_2 crystals [41].

3.2 Gas sensitivity properties

The gas sensing properties of the as-prepared mesoporous SnO_2 nanomaterials for ethanol were studied. Firstly, the

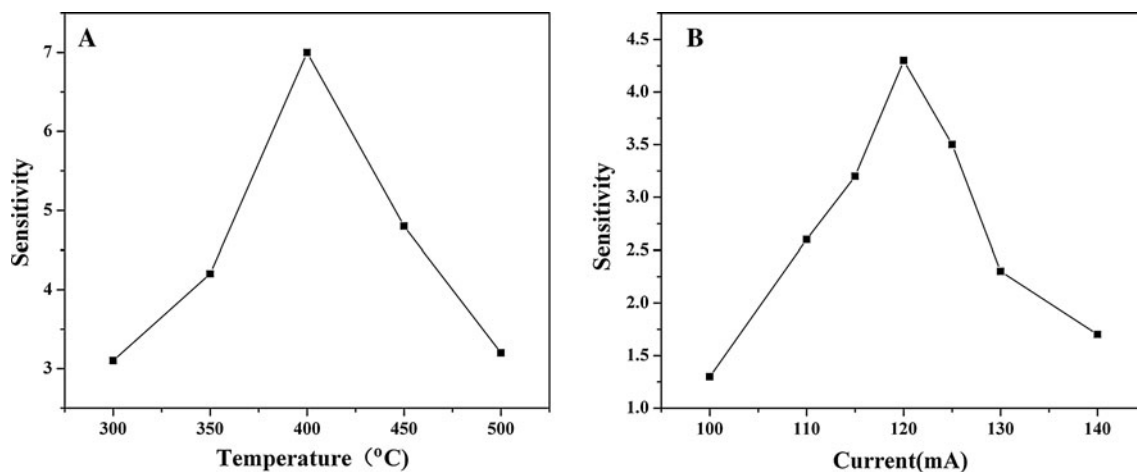


Fig. 6 **a** Sensor sensitivity versus calcining temperature of the synthesized mesoporous SnO_2 nanomaterials on 50 ppm ethanol and **b** Sensor sensitivity versus operating current of the mesoporous SnO_2 nanomaterials on 10 ppm ethanol

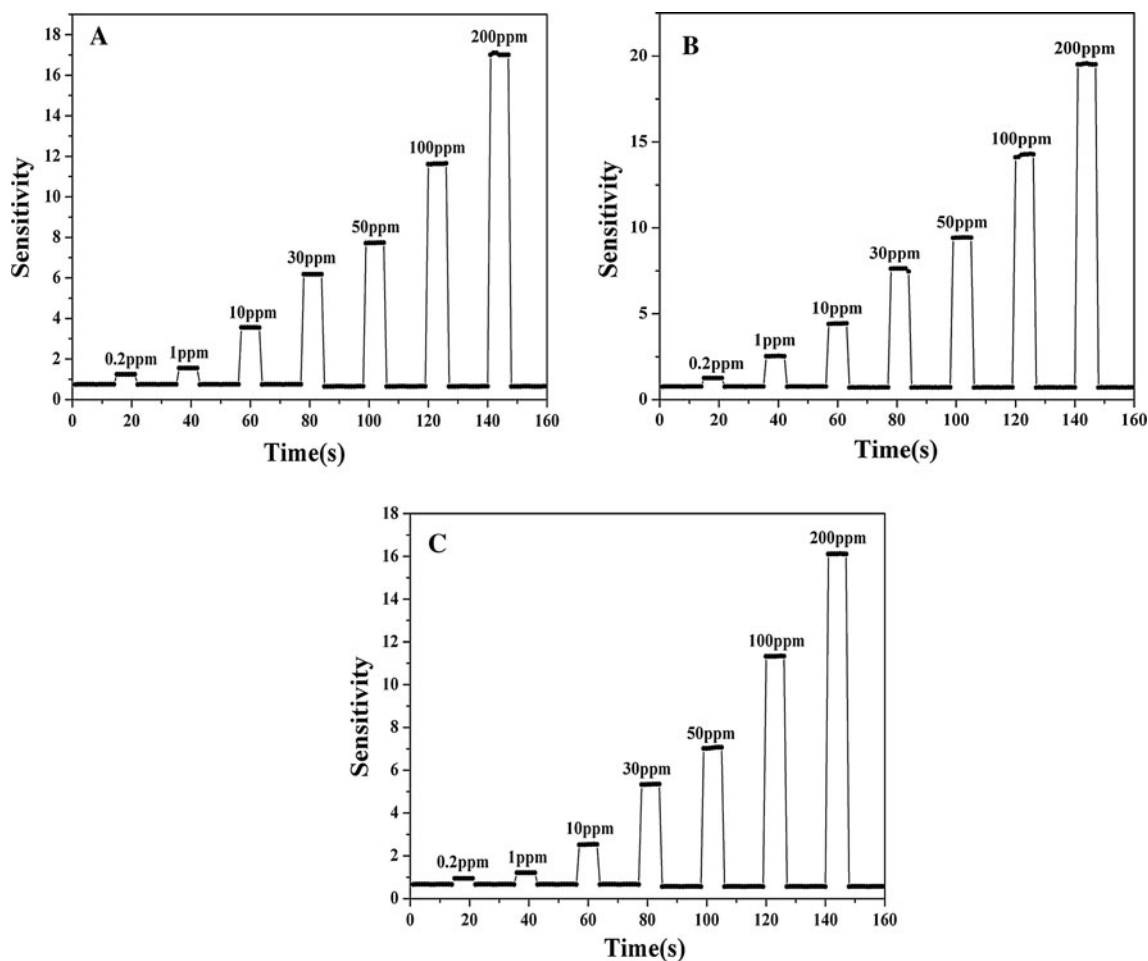


Fig. 7 Response of **a** SnO_2 -15, **b** SnO_2 -5 and **c** SnO_2 -6 sensors to 200 ppb–200 ppm ethanol

influence of calcining temperature on the sensing responses towards 50 ppm ethanol was investigated. The sensitivity varied with the calcining temperature is shown in Fig. 6a. From the curve, it can be seen that with the increase of the calcining temperature, the sensitivity increases. When the calcining temperature increases to 400 °C, the sensitivity reaches 7.0. Further increase of calcining temperature induces the sensitivity decrease obviously. Secondly, the effect of operating temperature on sensing responses towards 10 ppm ethanol was also investigated (Fig. 6b). From Fig. 6b, the sensitivity increases with the increase of operating temperature, until at 240 °C it reaches its maximum of 5.2. When exceed 240 °C, the sensitivity decrease obviously. From the above investigations, the calcinations at 400 °C and the operating temperature at 240 °C was used for all the samples in the follow experiments.

Figure 7 shows the sensitivity of SnO₂-15, SnO₂-5, and SnO₂-6 as the function of ethanol concentration. From the curves, it can be seen that the sensitivity of the sensor undergoes a drastic rise upon the injection of ethanol and

drops to its initial state after the sensor was exposed to air. As can be seen in Fig. 7a, the sensitivity of SnO₂-15 on 200 ppb ethanol is 1.2, the sensitivity increased to 17.0 as the concentration of ethanol was increased to 200 ppm. As shown in Fig. 7b, the sensitivity of SnO₂-5 on 200 ppb ethanol is 1.3, the sensitivity increased to 19.5 as the concentration of ethanol was increased to 200 ppm. Whereas, the sensitivity of SnO₂-6 (Fig. 7c) on 200 ppb ethanol is 0.9, the sensitivity increased to 16.1 as the concentration of ethanol was increased to 200 ppm.

From the above investigation, SnO₂-5 showed the highest sensitivity of all. Two main reasons are ascribed. One is the grain size effect of sample for sensitivity. It is known that, when $D \leq 2L$ (L is the thickness of the depletion layer), the gas sensing perform better. The $2L$ of SnO₂ ($L = 3$ nm) is 6 nm. From Fig. 4, the average particle size followed SnO₂-5 (4–6 nm) < SnO₂-6 (5–7 nm) < SnO₂-15 (7–9 nm). On the other hand, the surface area also plays an important party in the sensitivity. From Table 1, we can found that SnO₂-15 shows the largest surface area

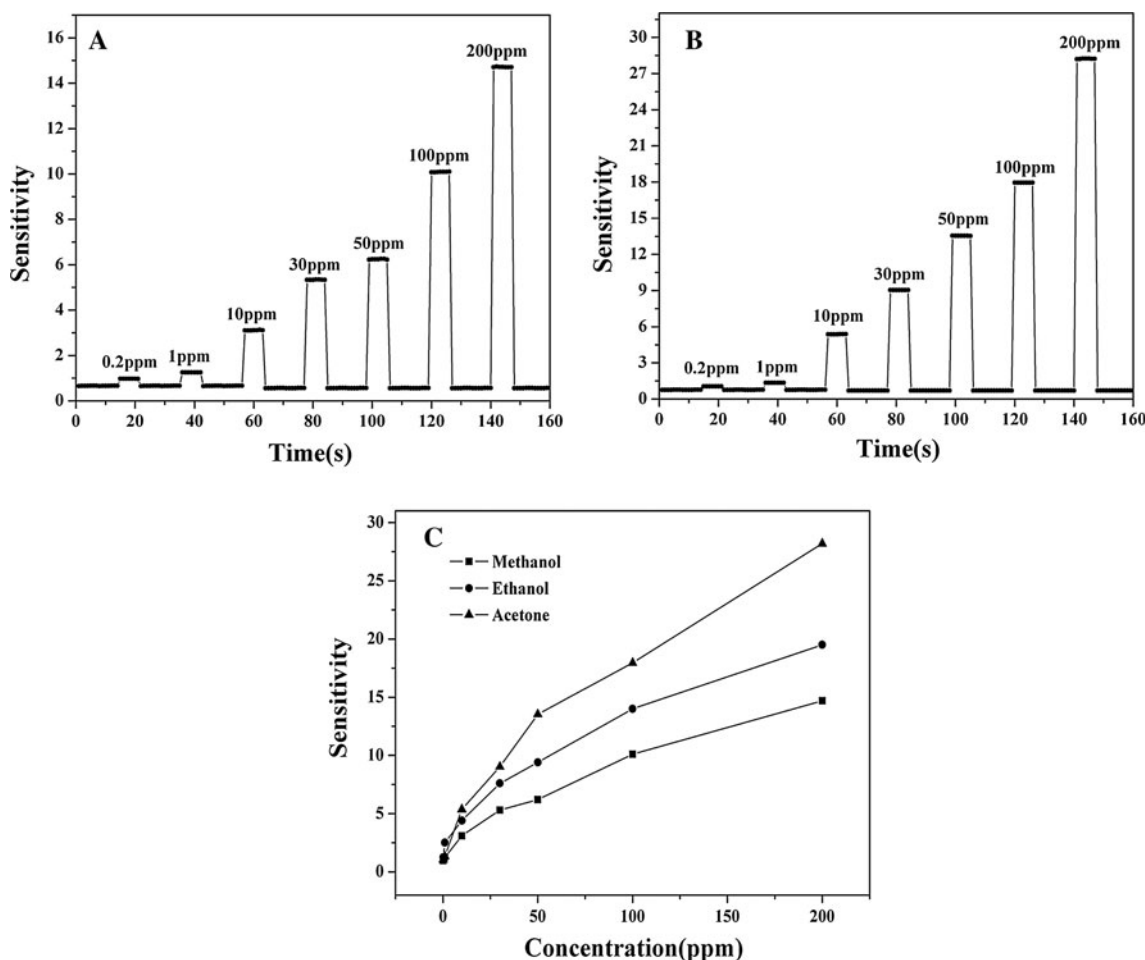


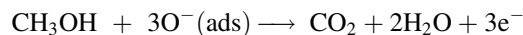
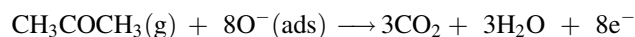
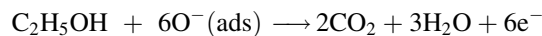
Fig. 8 Response of SnO₂-5 sensor to a 200 ppb–200 ppm methanol and b 200 ppb–200 ppm acetone, c Response of SnO₂-5 sensor to different concentrations of methanol, ethanol and acetone

($96 \text{ m}^2\text{g}^{-1}$), later is SnO₂-5 ($77 \text{ m}^2\text{g}^{-1}$), and SnO₂-6 possesses the lowest surface area ($57 \text{ m}^2\text{g}^{-1}$) among all. With smallest particle size (4–6 nm) and moderate surface area, SnO₂-5 shows the highest sensitivity. Although the grain size of SnO₂-15 is biggest, the largest surface area also makes SnO₂-15 show the excellent sensitive. From the above investigation, the mutual effect of grain size and the surface area determine the final sensitivity.

The response of SnO₂-5 to different concentrations of methanol and acetone are shown in Fig. 8a, b. The sensitivity increases with the increase of methanol and acetone concentration. The response slowly increases with increasing methanol and acetone concentration below 10 ppm. Above 10 ppm, the response rapidly increases with the methanol concentrations. As can be seen in Fig. 8a, the sensitivity of SnO₂-5 to 200 ppb methanol is 1.0, the sensitivity increased to 14.7 as the concentration of methanol was increased to 200 ppm. As shown in Fig. 8b, the sensitivity of SnO₂-5 is 1.3 at 200 ppb acetone, the sensitivity increased to 28.2 as the concentration of acetone

was increased to 200 ppm. As shown in Fig. 8c, the sensor exhibits the highest sensitivity to acetone than the others, implying a good response to acetone, three main reasons are ascribed.

1. Increases oxygen vacancies resulting CH₃COCH₃ amount, and thus greater reduced resistance of the material, significantly improving the sensitivity of the gas material on the CH₃COCH₃.



2. Good for gas sensing properties of acetone may be attributed to acetone gas contains two strong electron-withdrawing group, easier for SnO₂ adsorption,
3. Different required for gas distribution volume of liquid.

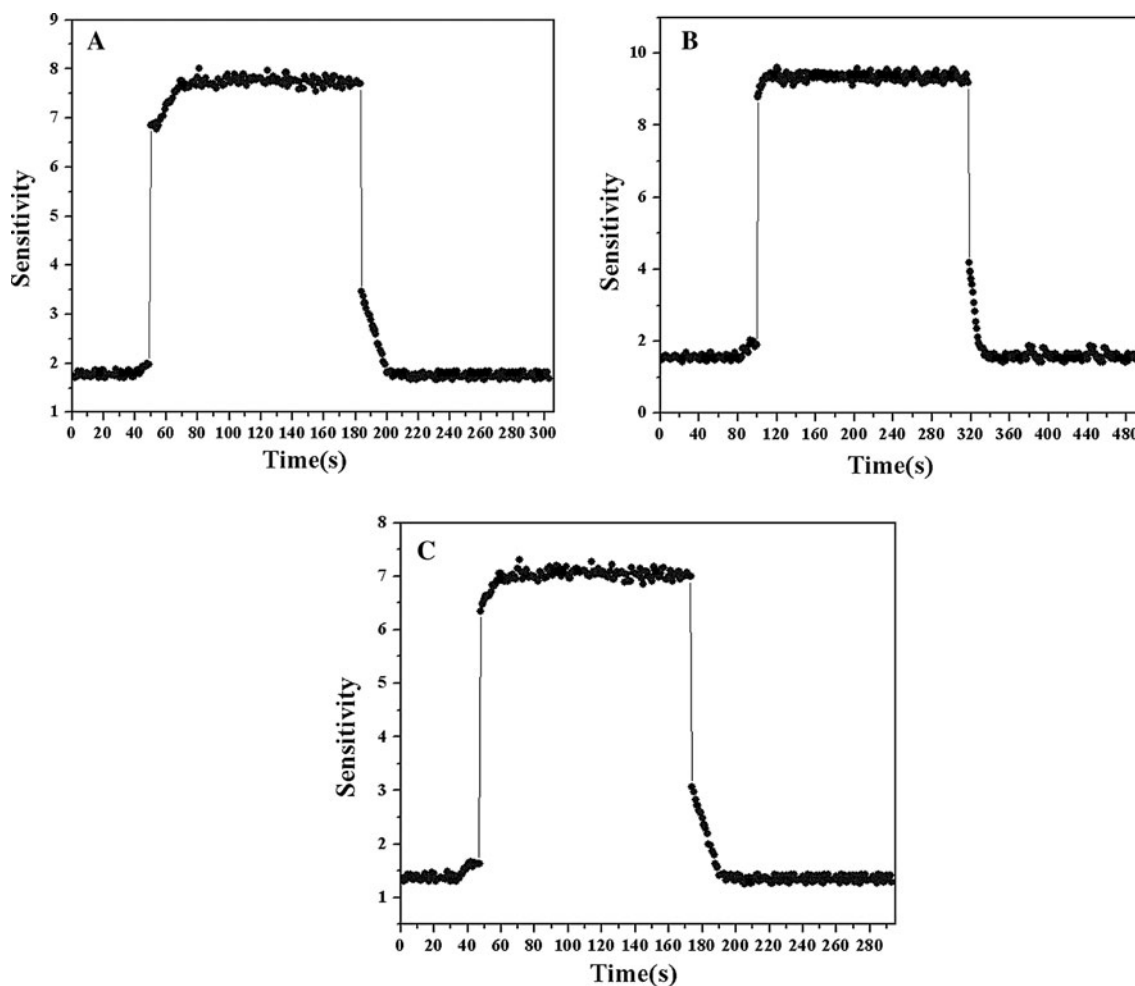


Fig. 9 Response and recovery curves of **a** SnO₂-15, **b** SnO₂-5 and **c** SnO₂-6 to 50 ppm ethanol

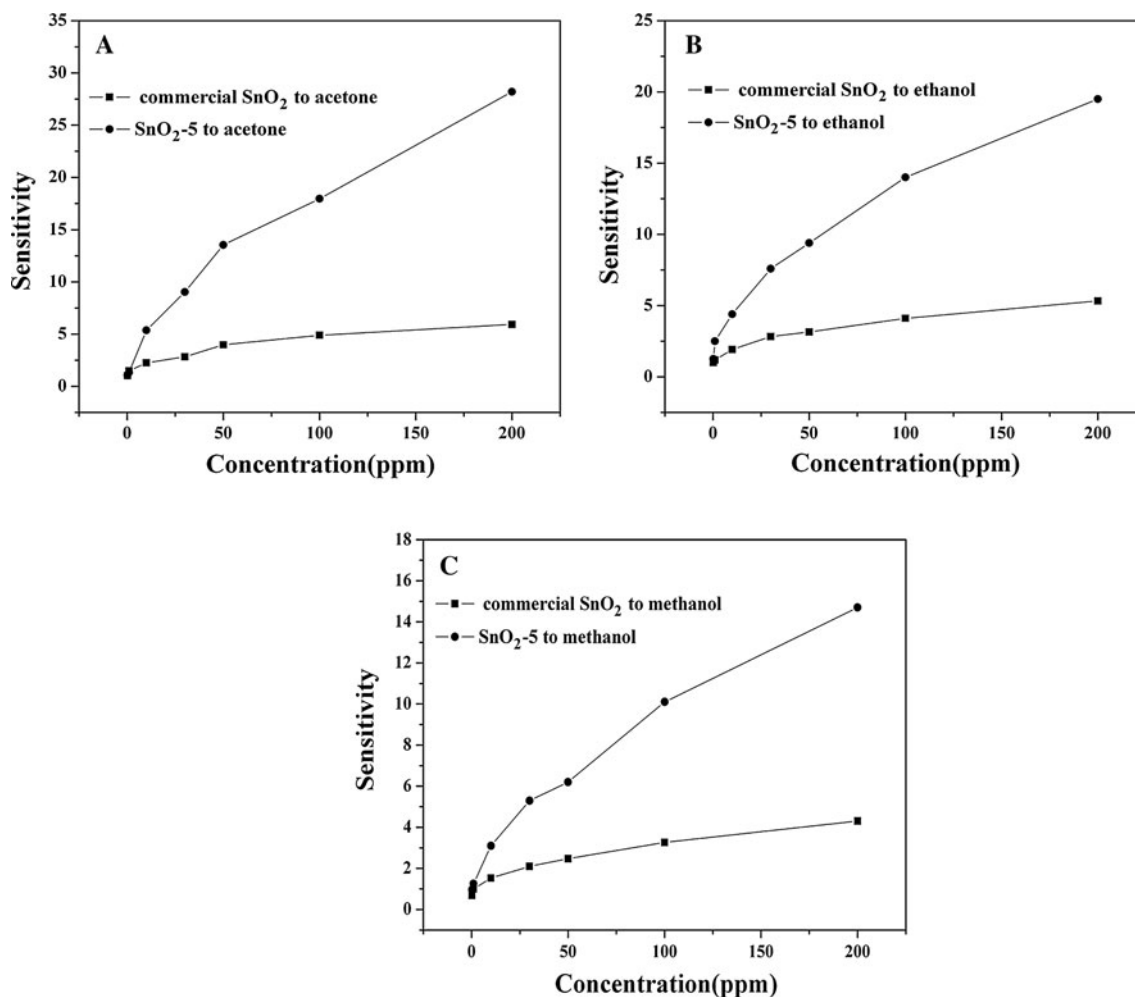


Fig. 10 Sensitivities of the SnO₂-5 and commercial SnO₂ powder based sensors to acetone, ethanol and methanol, respectively

As the molecular weight, density, we configured with 100 ppm ethanol, methanol, acetone, the desired volume of liquid, respectively: 5.2, 2.37, 6.62 μ L. Acetone is relatively large volume of liquid required.

In addition, the response and recovery time were also investigated for the mesoporous SnO₂ nanomaterials based sensors. The response and recovery times were 10.8 and 7.3 s for SnO₂-15, 8.7 and 6.5 s for SnO₂-5, 12.6 and 8.8 s for SnO₂-6, respectively, as shown in Fig. 9. It known that, KIT-5 and KIT-6 show the typical 3D structure. SnO₂-5 and SnO₂-6 templated from KIT-5 and KIT-6 also show the 3D structure characters. From the data, SnO₂-5 shows the fastest response due to their 3D structure, which facilitates the diffusion of gas molecules. Although SnO₂-6 also possesses 3D porous structure, the low surface area limits the response.

In order to evaluate the performance of these mesoporous SnO₂ on sensors, commercial SnO₂ powder was used for contrast (Fig. 10). From Fig. 10a, the response of commercial SnO₂ powder is 5.9 (acetone 200 ppm),

whereas SnO₂-5 sensor is 28.2. As can be seen in Fig. 10b, at ethanol concentration of 200 ppm, the response of commercial SnO₂ powder is 5.3, whereas SnO₂-5 sensor is 19.5. As shown in Fig. 10c, the response is 4.3 and 14.7 for commercial SnO₂ and SnO₂-5 at 200 ppm methanol. With the special mesoporous structure, show the SnO₂-5 exhibits the obviously enhanced sensitivity compared with commercial SnO₂ powder.

The long-time stability of this sensor was investigated by repeating the test after aging. Figure 11 shows the sensitivity of the sensor to 200 ppm methanol, ethanol and acetone within 100 days. As shown in Fig. 11, the mesoporous SnO₂ nanomaterials shows the well stability for the three gases after 100 days.

3.3 Gas sensor mechanism

The sensing mechanism of sensors can be explained as follows.

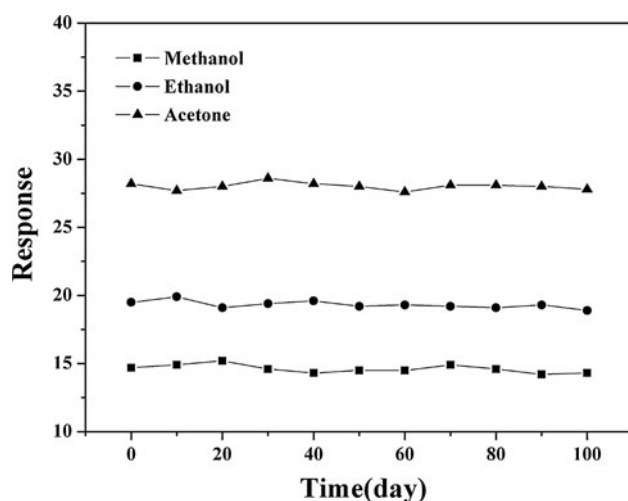
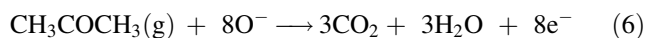
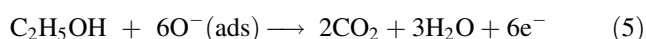
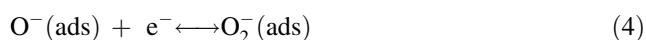
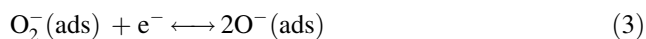


Fig. 11 Stability of SnO₂-5 to 200 ppm methanol, ethanol and acetone

N-type semiconductor adsorbed oxygen molecules in the air, the oxygen molecules trapping electron in the surface of the semiconductor, thereby forming oxygen anions (O^- , O^{2-}), this results in an increase in resistance semiconductor surface. When the measured gas in contact with the semiconductor surface and react with the adsorbed oxygen, electron captured by oxygen to return to the semiconductor, then resistance is reduced, such significant changes in the resistance of the semiconductor on the realization of the gas detection.

The related reactions are expressed as follows:



4 Conclusions

Mesoporous SnO₂ nanomaterials were synthesized by replicate hard templates SBA-15/KIT-5/KIT-6, respectively. These mesoporous SnO₂ nanomaterials showed high BET surface areas and pore volume. The corresponding BET surface areas and pore volumes for SnO₂-15, SnO₂-5 and SnO₂-6 are 96 m²g⁻¹ and 0.21 cm³g⁻¹, 77 m²g⁻¹ and 0.27 cm³g⁻¹, and 57 m²g⁻¹ and 0.17 cm³g⁻¹, respectively. In particular, SnO₂ nanoparticles show a strong size-

induced enhancement of gas sensing performance. The response of SnO₂-15, SnO₂-5, and SnO₂-6 are 17.0, 19.5, 16.1, respectively as the concentration of ethanol on 200 ppm. The SnO₂-5 exhibit a four fold enhancement in sensitivity compared to commercial SnO₂ powder on acetone. With the large surface area and small particle size, SnO₂-5 showed the best response of all. The mesoporous SnO₂ nanomaterials exhibit low detection limit (ppb level), a complete and fast recovery to its initial state, and long-term sensing stability, this could be ascribed to the grain size, the surface areas, and the porous structure. With the large surface area, and particle size, these mesoporous SnO₂ nanomaterials have potential application on catalysis, adsorption and batteries.

Acknowledgments Financial support for this study was provided by the National Natural Science Foundation of China (21171045, 21101046), Natural Science Foundation of Heilongjiang Province of China ZD201214, Program for Scientific and Technological Innovation team Construction in Universities of Heilongjiang province (2011TD010), Doctoral Initiation Fund of Harbin Normal University (20102329110002), Foundation of Harbin Educational Committee (12521164).

References

- Kresge CT, Leonowicz ME, Roth WJ, Vartulli JC, Beck JS (1992) *Nature* 359:710–712
- Beck JS, Vartulli JC, Roth WJ, Leonowicz ME, Schmitt KD, Olson DH, Sheppard EW, NcCullen SB, Higgins JB, Schlenker JL (1992) *J Am Chem Soc* 114:10834–10843
- Scott BJ, Wirmsberger G, Stucky GD (2001) *Chem Mater* 13:3140–3150
- Wark M, Rohlffing Y, Altindag Y, Wellmann H (2003) *Phys Chem Chem Phys* 5:5188–5194
- Bhat SD, Naidu BVK, Shanbhag GV, Halligudi SB, Sairam M, Aminabhavi TM (2006) *Sep. Pur. Technol* 49:56–63
- Jiang Q, Wu ZY, Wang YM, Cao Y, Zhou CF, Zhu JH (2006) *J Mater Chem* 16:1536–1542
- Zhai QZ, Hu WH, Huang BL, Wang CY (2012) *J Sol-Gel Sci Technol* 63:435–444
- Li GJ, Kawi S (1999) *Sens Actuators B* 59:1–8
- Gierszal KP, Kim TW, Ryoo R, Jaroniec M (2005) *J. Phys. Chem. B* 109:8774–8778
- Zhao D, Huo Q, Feng J, Chmelka BF, Stucky GD (1998) *J Am Chem Soc* 120:6024–6036
- Chang SC, Huang MH (2008) *J Phys Chem C* 112:2304–2306
- Wagner T, Waitz T, Roggenbuck J (2007) *Thin Solid Films* 515:8360–8363
- Liu Z, Zhang D, Han S, Li C, Tang T, Jin W, Liu X, Lei B, Zhou C (2003) *Adv Mater* 15:1754–1757
- Liu Y, Dong J, Liu M (2004) *Adv Mater* 16:353–356
- Dai ZR, Pan ZW, Wang ZL (2002) *J Am Chem Soc* 124:8673–8680
- Hu JQ, Ma XL, Shang NG, Xie ZY, Wong NB, Lee CS, Lee ST (2002) *J. Phys. Chem. B* 106:3823–3826
- Waghoo G, Jayaram RV, Joshi MV (1999) *Synth Commun* 29:513–520
- Dimitrov M, Tsoncheva T, Shao SF, Koehn R (2010) *Appl Catal B* 94:158–165

19. Ye Q, Wang J, Zhao JS, Yan LN, Cheng SY, Kang TF, Dai HX (2010) *Catal Lett* 138:56–61
20. Katsuki A, Fukui K (1998) *Sens Actuators B* 52:30–37
21. Yin XM, Li CC, Zhang M, Hao QY, Liu S, Li QH, Chen LB, Wang TH (2009) *Nanotechnology* 20:455503–455507
22. Firooz AA, Mahjoub AR, Khodadadi AA (2009) *Sens Actuators B* 141:89–96
23. Choi YJ, Hwang IS, Park JG, Choi KJ, Park JH, Lee JH (2008) *Nanotechnology* 19:095508
24. Liu Y, Koep E, Liu ML (2005) *Chem Mater* 17:3997–4000
25. Zhang J, Liu XH, Wu SH, Xu MJ, Guo XZ, Wang SR (2010) *J Mater Chem* 20:6453–6459
26. Oliaee SN, Khodadadi A, Mortazavi Y, Alipour S (2010) *Sens Actuators B* 147:400–405
27. Park JA, Moon J, Lee SJ, Kim SH, Chu HY, Zyung T (2010) *Sens Actuators B* 145:592–595
28. Jain K, Pant RP, Lakshmikummar ST (2006) *Sens Actuators B* 113:823–829
29. Moon WJ, Yu JH, Choi GM (2001) *Sens Actuators B* 80:21–27
30. Wu X, Sui JH, Cai W, Qu FY (2008) *Mater Chem Phys* 112:325–328
31. Han YT, Wu X, Shen GZ, Gong LH, Qu FY, Bando Y, Sekiguchi T, Fabbri F, Golberg D (2010) *J Phys Chem C* 114:8235–8240
32. Han YT, Wu X, Ma YL, Gong LH, Qu FY, Fan HJ (2011) *Cryst Eng Commun* 13:3506–3510
33. Liu SQ, Xie MJ, Li YX, Guo XF, Ji WJ, Ding WP (2010) *Mater Chem Phys* 123:109–113
34. Zhao DY, Feng J, Huo Q, Melosh N, Fredrickson GH, Chemlka BF, Stucky GD (1998) *Science* 279:548–552
35. Kim TW, Kleitz F, Paul B, Ryoo R (2005) *J Am Chem Soc* 127:7601–7610
36. Kleitz F, Liu D, Anilkumar GM, Solovyov LA, Shmakov AN, Ryoo R (2003) *J. Phys. Chem. B* 107:14296–14300
37. Zhang Y, He XL, Li JP, Miao ZJ, Huang F (2008) *Sens Actuators B* 132:67–73
38. Ryoo R, Joo SH, Kruk M, Jaroniec M (2001) *Adv Mater* 13:677–681
39. Wu HB, Chen JS, Lou XW, Hng HH (2011) *J Phys Chem C* 115:24605–24610
40. Torchynska TV, Hernandez AV, Cano AD, Sandoval SJ, Ostapenko S, Mynbaeva M (2005) *J Appl Phys* 97:33507
41. Xu J, Li YS, Huang HT, Zhu YG, Wang ZR, Xie Z, Wang XF, Chen D, Shen GZ (2011) *J Mater Chem* 21:19086–19092